A comparative study of the effect of submicron porous and smooth ultrafine-grained Ti-20Mo surfaces on osteoblast responses

N. Gui[1], W. Xu[1, 2, 3*] A. N. Abraham[4], D. E. Myers[5, 6], E. L.H. Mayes[7], K. Xia[3], R. Shukla[4], and M. Qian[1*]

[1] Centre for Additive Manufacturing, School of Engineering, RMIT University, Melbourne, VIC 3000, Australia

[2] School of Engineering, Macquarie University, Sydney, NSW 2109, Australia

[3] Department of Mechanical Engineering, University of Melbourne, VIC 3010, Australia

[4] Nanobiotechnology Research Laboratory and Centre for Advanced Materials & Industrial Chemistry, School of Science, RMIT University, Melbourne, VIC 3001, Australia

[5] Australian Institute for Musculoskeletal Science, Victoria University and University of Melbourne, Australia

[6] College of Health and Biomedicine, Victoria University; Western Centre for Health and Research Education, Sunshine Hospital, VIC 3021, Australia

[7] RMIT Microscopy and Microanalysis Facility (RMMF), GPO Box 2467V, Melbourne VIC 3000, Australia

*Corresponding authors:

ma.qian@rmit.edu.au;

wei.xu@mq.edu.au

Abstract:

The surface of an orthopaedic implant plays a crucial role in determining the adsorption of proteins and cell functions. A detailed comparative study has been made of the *in vitro* osteoblast responses to coarse-grained (grain size: 500 μm), ultrafine-grained (grain size: 100 nm), coarse-porous (pore size: 350 nm) and fine-porous (pore size: 155 nm) surfaces of Ti-20Mo alloy. The purpose was to provide essential experimental data for future design of orthopaedic titanium implants for rapid osseointegration. Systematic original experimental data was produced for each type of surfaces in terms of surface wettability, cell morphology, adhesion, growth and differentiation. Microscopic evidence was collected to reveal the detailed interplay between each characteristic surface with proteins or cells. Various new observations were discussed and compared with literature data. It was concluded that the coarse-porous surfaces offered the optimum topographical environment for osteoblasts and that the combination of ultrafine grains and considerable grain boundary areas is not an effective way to enhance cell growth and osteogenic capacity. Moreover, pore features (size and depth) have a greater effect than smooth surfaces on cell growth and osteogenic capacity. It proves that cells can discern the difference in pore size in the range of 100-350 nm.

Keywords: Ti-20Mo, ultrafine grains, submicron porous surfaces, osteoblast responses, filopodia

INTRODUCTION

Titanium (Ti) and its alloys are the materials of choice for orthopaedic implants due to their advantageous attributes including high biocompatibility, excellent corrosion resistance in bodily fluids, high strength-to-weight ratios, high fracture toughness and good fatigue properties [1, 2]. Up till now, commercially pure Ti (CP-Ti) and Ti-6Al-4V (in wt.% unless otherwise stated) remain the most widely used Ti alloys for biomedical applications (CP-Ti is mainly used for dental applications). However, these alloys have much higher Young's modulus (~110 GPa) than cortical bones (10-30 GPa), leading to the so-called stress shielding effect [3]. Another concern on orthopaedic implants made from Ti-6Al-4V is the release of toxic Al and V ions from the surface [1].

Consequently, a significant effort has been made for the development of Al- and V-free low-modulus beta-type Ti alloys (β-Ti) [3], where β-Ti alloys refer to those that can retain 100% of the β-phase on water quenching due to the β-stabilizing effect of alloying elements such as molybdenum (Mo), niobium (Nb), tantalum (Ta) and iron (Fe) [4]. The minimum amount of Mo required for this purpose is 10 wt.% [5]. On this basis, the so-called "Mo equivalency" has been commonly used to evaluate the β-phase stability in a Ti alloy for both alloy design and microstructural control [5].

As a non-toxic potent β-stabilizer, Mo has long been used as a principal alloying element for the development of biocompatible low-modulus β-Ti alloys [6]. In addition, Mo is an essential component of certain enzymes and therefore plays an important role in balancing the pH values in human body [7, 8]. As a result, binary Ti-Mo alloys have been studied extensively for biomedical applications [3, 9-11]. One such notable development is the compositionTi-15Mo, which is available commercially today in various product forms [12] under ASTM F2066 for high-strength bone implant applications [13]. Ti-15Mo is currently produced in two types of microstructures, namely, single β-phase and β + α [12]. The (β + α)-Ti-15Mo, which takes advantage of the metastability of its β-phase for α to precipitate due to the insufficient Mo content (15%), offers both high strengths (desired) and modulus (undesired) compared to the single β-phase Ti-15Mo. In order to ensure the achievement of a full β-phase Ti-Mo alloy under a broad range of processing conditions, rather than restricted to water quenching, it is necessary to further enhance the β-phase stability, i.e., to increase the Mo content. In this regard, metastable β-Ti-20Mo alloy has emerged as a promising choice with Young's modulus of 91 GPa [8, 14-17]. In particular, Bolat et al. have recently shown that Ti-20Mo displayed excellent corrosion resistance in saline solutions [14], implying good potential for orthopaedic applications. Accordingly, Ti-20Mo is chosen as the experimental alloy for this study.

Rapid and long-lasting osseointegration is crucial to the clinical success of an implant [18]. The surface of an orthopaedic implant plays a crucial role in determining the adsorption of proteins and cell functions such as adhesion, proliferation and differentiation [19, 20]. The interactions occur from microscale down to nanoscale [18, 21]. As such, various approaches have been used to modify Ti

surfaces for enhanced biofunctionality. For example, achieving an ultrafine-grained surface has proved effective in enhancing the biocompatibility with cells compared to the coarse-grained surface of the same alloy [22-26]. In addition, an ultrafine-grained Ti alloy can effectively reduce the size or wall thickness of orthopaedic implants due to strengthening by grain refinement [27, 28]. With regards to the elastic modulus, which is an important implant property, in general, achieving an ultrafine grain size has no effect unless the grain size is reduced to about 20 nm below which the elastic modulus decreases with decreasing grain size [29-32]. However, it should be pointed out that for metastable β-Ti alloys such as Ti-Mo alloys, if the ultrafine grain size is achieved by severe plastic deformation and accompanied by significant formation of stress-induced ω-phase particles, then the elastic modulus can increase due to the ω-phase [33].

Another commonly used surface modification approach for implants is the introduction of an interconnected porous surface, which offers distinct advantages over dense surfaces. These include: (i) reduced Young's modulus at the specific area of contact [1, 2, 34], (ii) enabling bone ingrowth [35-37], and (iii) easy distribution of nutrients for cell growth [38]. Pore size and pore interconnectivity have been documented as the two main factors that need to be considered in the design of such a porous surface [1, 39].

Although both ultrafine-grained and interconnected porous surfaces can enhance cell responses, it remains elusive as to which surface features are more effective in regulating cell functions. A detailed literature survey has found no relevant *in vitro* comparative studies on ultrafine-grained surfaces vs. interconnected porous surfaces. Thus, this study systematically compares osteoblast cell responses to both ultrafine-grained (grain size: ~100 nm) and submicron porous (pore size: 150-350 nm) surfaces of Ti-20Mo. The porous surface features ranging from 100-400 nm are selected because of their similarity in length scale to that of filopodia (100-300 nm) [40]. The purpose is to investigate how surface topography and wettability affect cell attachment, adhesion, growth and differentiation. The outcomes are expected to form an essential knowledge base for the design of Ti-20Mo alloy as orthopaedic implants.

MATERIALS AND METHODS

Fabrication and preparation of substrates

The fabricated Ti-20Mo alloy substrates with a diameter of 10 mm and a thickness of 1 mm were used in this study. As-cast Ti-20Mo alloy samples were first solution-treated at 1273K for 48 h, followed by water quenching to produce metastable β-Ti-20Mo microstructures, denoted as coarse grained. To obtain the ultrafine-grained microstructure, high pressure torsion (HPT, a severe plastic deformation technique for grain refinement) was applied to the water-quenched Ti-20Mo substrates under a pressure of 6 GPa for 10 turns, and the substrates thus produced are referred to as ultrafine grained. For further details regarding HPT technique the reader is referred to the published work by Xu et al.[16] and one comprehensive review by Zhilyaev et al.[41].

All the disks were ground first with SiC sandpaper from P320 to P4000 and then polished using a mixture of OPS colloidal silica (0.04 μm) and 10% hydrogen peroxide (H_2O_2). The prepared disks were cleaned with acetone, ethanol and distilled water in ultrasonic bath for 15 min at each step, and dried with N_2 gas. Finally, for producing interconnected pores on the surfaces, the ultrafine-grained substrates were heat-treated (aging) at 550 °C for up to 60 min under Ar atmosphere followed by water quenching. The Kroll's reagent (HF: 2ml, HNO_3: 6 ml, distil water: 92 ml) was then used to etch the polished substrates for 1 min. The creation of interconnected pores was achieved by removing the α (Mo-depleted) phase from the duplex structures via acid etching and only leaving the β (Mo-rich) phase [16]. The acid-etched substrates that were aged for 0 min (no holding) are denoted as fine porous. In addition, after prolonging the aging period to 60 min and acid etching, coarser pores were obtained on the surface, named as coarse porous. In this study, the coarse-grained Ti-20Mo (without HPT, aging and acid-etching) is treated as a control. Table 1 summarizes the fabrication processes of all the substrates.

Grain structure and surface characterisation

X-ray diffraction (XRD) patterns of all Ti-20Mo substrates were measured using a Bruker D4 diffractometer, which is equipped with a Cu source. X-ray photoelectron spectroscopy (XPS) of all Ti-20Mo substrates was carried out using a Thermofisher Scienfitic K-Alpha system with an Al kα source and a spot size of 400 μm. The grain structures of both coarse-grained and ultrafine-grained surfaces were examined by a transmission electron microscope (TEM).

Surface morphology was evaluated using an ultra-high-resolution scanning electron microscope (SEM, FEI, Verios 460L). The measurement of the pore diameter distribution was analysed from measuring at least 100 pores on three different locations for each sample using both the line and ROI manager tools in *Image J*. Three samples were measured from each group. Focused ion beam (FIB, FEI, Scios) milling was employed to cut through the surface to observe the pore depths and profiles. Surface roughness characterised by the average roughness (S_a) and root mean square roughness (S_q) were measured using an AFM (Bruker) in the tapping mode. Each AFM analysis was performed over an area of 3 μm × 3 μm. To ensure the representativeness of the surface characteristics, three samples were selected from each group and three different areas were scanned in each sample.

Surface wettability was measured by the sessile-drop contact angle method (Theta Lite Optical Tensiometer, ATA Scientific). Two different solvents were applied: ultrapure distilled water and ethylene glycol. The contact angle was measured at 5 s after placing the droplet (2 μL) on the surface of each sample and repeated at three different areas of the sample. The tests were applied to three different samples selected from each group. The surface free energy (γ) and its components were calculated using the Owens-Wendt (OW) method , given in Eq.1: [42]

$$\gamma_L(1+cos\theta) = 2\sqrt{\gamma_L^d \gamma_S^d} + 2\sqrt{\gamma_L^p \gamma_S^p} \quad (1)$$

where γ_L is the surface tension of the liquid; γ_S is the surface energy of the solid; and γ_S is the sum of the dispersion component (γ^d) and the polar component (γ^p). γ_L, γ^p and γ^d for water are 72.8, 51.0, and 21.8 mJ/m^2, respectively [42], and 48.0, 19.0, and 29.0 mJ/m^2, respectively for ethylene glycol.

Cell culture

Human fetal osteoblast line (hFOB 1.19) was used in this study (ATCC, CRL-11372). They were cultured in the medium of mixed Dulbecco's Modified Eagle's and Ham's F12 (DMEM/F12, Thermofisher Scientific), added with 10 % (v/v) fetal bovine serum (FBS, Interpath Services) and 0.3 mg/ml Geneticin selective antibiotics G418 (Thermofisher Scientific) at 34˚C in a humidified atmosphere of 5% CO_2. The complete growth medium was replaced every 3 days and confluent cells were subcultured using TrypLE™ Express Enzyme (Invitrogen). When cells were confluent, a total of 3×10^5/200 µl cells were seeded on each disk in a 24-well culture plate for the study of cell number and differentiation. For imaging cell morphology, cells were seeded at a density of 2×10^5/200 µl on each disk in a 24-well plate. The culture medium was replenished every 3 days.

Immunofluorescence observation of cell morphology and focal adhesions (FAs)

After culturing for 8 days, the cell-seeded disks were washed with phosphate buffered saline (PBS), fixed with 4% paraformaldehyde solution in PBS for 10 min. Cells were permeabilized with 0.02 % (v/v) Triton X-100 in PBS for 90 s and blocked with 2 % (wt/v) bovine serum albumin (BSA) in PBS for 30 min. Vinculin was immunostained by incubating cells in 1:50 dilution of mouse monoclonal lgG antibody (anti-vinculin) (Santa Cruz Biotechnology) in blocking buffer (i.e., the BSA) for 1 h. Subsequently, cells were washed and probed with goat-anti-mouse secondary antibody Alexa Fluor 594 conjugate (Invitrogen, 1:500) in blocking buffer for 45 min. Following extensive washing steps to remove free secondary antibody, actin filaments were stained with 1:40 dilution of Oregon Green 488 phalloidin in blocking buffer for 20 min. Cell nuclei were stained with Hoechst 33342 (2 µg/ml in PBS) for 10 min. Finally, all disks were mounted onto cover glasses with gold anti-fade mounting medium and imaged using a confocal microscope (N–STORM,

Nikon). Images were collected at three locations on each substrate using a confocal microscopy. Moreover, the distribution of vinculin, cell spreading area and cell elongation ratio (the ratio of cell long axis and short axis) were quantified using *Image J* (version 1.6) [43]. For each substrate, approximately 25 cells were analysed with two replicates. The confocal images taken using an objective of 40× were utilized to quantify the effect of surface features on the length of FAs. The captured immunofluorescence images were first split into single-channel greyscale images. Afterwards, all greyscale images of FAs were adjusted in terms of brightness and contrast and then thresholded, both particle analysis and ROI manager tools were employed to evaluate the length of FAs on each substrate [44, 45]. For measuring cell spreading area and elongation ratio of osteoblasts, polygon and line tool and ROI manager of *Image J* were used.

Cell morphology using SEM

Cell morphology was studied on various Ti-20Mo disks using a SEM. After culturing for 1 day, cell-seeded disks were rinsed with sodium cacodylate and then fixed with 0.1M cacodylate buffer that contains 2 % (v/v) paraformaldehyde and 2.5 % (v/v) glutaraldehyde for 30 min. They were dehydrated in a graded series of ethanol (from 30% to 100%). [46]all substrates were chemically dried with 100% hexamethyldisilazane (Sigma-Aldrich) for 20 min. Prior to SEM imaging, all samples were sputter-coated with platinum (Pt). Secondary electron images were collected with an accelerating voltage of 2 kV. For quantifying the length of filopodia and cell spreading areas, SEM images were analysed using line and polygon tool and ROI manager of *Image J* on two samples from each group.

Cell number and alkaline phosphatase (ALP) activity

Cell numbers were measured by directly counting using a haemocytometer. After culturing for 8 days, all the disks were transferred to other sterilized 24-well plates. After washing with PBS once, the adhered cells were detached from the surfaces of the disk samples with 200 µl of TrypLE™. The cell suspensions were collected in eppendorf tubes and placed on ice before

centrifuging at 1000 rpm for 5 min. Adhered cell number was determined by counting using the standard trypan blue exclusion method.

ALP activity is an early osteogenic differentiation indicator, measured using an ALP fluorescence detection kit (Sigma-Aldrich). The principle of this kit is to hydrolyze *p*-nitrophenyl phosphatase to *p*-nitrophenol at 37 °C [47]. Cells were cultured on disks for 8 days at an initial seeding density of 3×10^5 cells/ well. The adhered cells were lysed with 0.2 % (v/v) Triton X-100 for 10 min and cell lysates were collected in eppendorf tubes and centrifuged at 12,000 rpm for 5 min at 4 °C. Supernatants of cell lysates were transferred into new eppendorf tubes, stored at −80°C until used. Cell lysates were used to measure the ALP activity. Fluorescence intensity was measured at an excitation wavelength of 360 nm and an emission wavelength of 440 nm using a microplate reader (SpectraMax Paradigm, Molecule device). The total protein content was determined by a BCA protein assay kit (Pierce) following manufacturer's instructions and the absorbance was measured by a microplate reader. The ALP activity was normalized by the total protein content.

Statistical analysis

Statistical analysis was performed using one-way analysis of variance (ANOVA), with post hoc testing using Turkey's multiple comparison tests (GraphPad Prism). Data were expressed in the form of mean value ± standard deviation (SD). A value of $p < 0.05$ was considered significant.

RESULTS

Grain structure and surface characteristics

The grain structures of coarse-grained and ultrafine-grained substrates were characterised using either a SEM or a TEM, as shown in Fig. 1. The average grain size of the coarse-grained substrate is 507 ± 87 μm, while that of the ultrafine-grained substrates is 104 ± 22 nm. Average roughness S_a and root mean square roughness S_q (0.3-1.1 nm) of coarse-grained and ultrafine-grained substrates are listed in Table 2. Both coarse-grained and ultrafine-grained substrates were

smooth and flat at the nanoscale. Fig. 2 shows XRD profiles of the four Ti-20Mo substrates. Both the coarse-grained and ultrafine-grained substrates are composed of β phases, while both the fine-porous and coarse-porous substrates consist of a mixture of α and β phases. Fig. 3 shows submicron interconnected pores in the surface layers of both fine-porous and coarse-porous surfaces. The coarse-porous substrate (aged at 550 °C for 60 min, Figs. 3E-G) contained coarser pores, of a mean diameter of 350 ± 96 nm compared to 155 ± 38 nm in the fine-porous substrate (aged at 550 °C for 0 min, Figs. 3A-C). This is because increasing aging time from 0 min (fine porous) to 60 min (coarse porous) leads to an increase in the size of α precipitates [16] which are subsequently etched away to form coarser pore cavities. The average pore sizes (~155 nm for fine-porous and ~350 nm for coarse-porous surfaces) are far larger than the average sizes of the α phase (<100 nm for fine-porous and ~200 nm for coarse-porous surfaces) [16], indicative of a complete removal of α phases. In addition, surface composition analysis using XPS showed a substantial increase in Mo from 18 wt.% for coarse-grained and ultrafine-grained surfaces to more than 30 wt.% for fine-porous and coarse-porous surfaces (Table 3). This also suggests that the entire α phase and a portion of the β matrix have been removed by etching to form the porous surface structures of the fine-porous and coarse-porous substrates. Moreover, the analysis on the cross section of the porous surface structures using a dual beam FIB/SEM (Fig. 8) revealed an average pore depth of 0.95 ± 0.12 μm for the fine-porous surfaces, which was nearly half that of 1.95 ± 0.25 μm for the coarse-porous surfaces. Table 2 summarises the pore size and the thickness of the porous surface layer for both the fine-porous and coarse-porous surfaces.

Fig. 4 shows the contact angle (θ) values of ultrapure distilled water measured on each surface and the corresponding water droplet morphology. Coarse-grained and fine-grained surfaces demonstrated similar contact angles (58.23 ± 6.28° vs. 61.66 ± 7.76°). However, much lower contact angles were observed for both fine-porous (27.86 ± 4.11°) and coarse-porous (39.33 ± 8.24°) surfaces. Table 4 summarises the surface free energy values obtained for each surface. Both the total surface free energy and its relevant polar component of the fine-porous and coarse-porous

surfaces are about twice the respective values of coarse-grained and ultrafine-grained surfaces. In contrast, a substantial grain size reduction from 500 μm to 100 nm led to merely a marginal increase of 24% in total surface free energy (i.e., better wettability) (Table 4). Being porous was therefore much more effective in enhancing the wettability than grain refinement.

Cell morphology and adhesion

The osteoblast morphology on each substrate surface was investigated using both SEM and confocal microscopy at different times of culturing. Fig. 5 shows representative SEM images of osteoblasts on each surface after culturing for 1 day. Cells spread more broadly on both coarse-grained and ultrafine-grained surfaces than on fine-porous and coarse-porous surfaces. In addition, both the cell nuclei and grown cells were nearly spherical on fine-porous and coarse-porous surfaces. Figs. 5 (B, D, F, H) are higher magnification views of the filopodia corresponding to Figs. 5 (A, C, E G). Filopodia integrated themselves well into both fine pores and coarse pores on the surfaces.

Fig. 6 show a closer view of the interactions between the filopodia and pores on the fine-porous surfaces. The filopodia interacted with submicron pores (~155 nm) intensively at different depths and eventually grew into these pores (indicated by arrows in Fig. 6). In order to further gauge the interactions between osteoblasts and implant surfaces, a quantitative measurement of cell morphology was conducted using *Image J*. Both the average length of filopodia and the average cell spreading area were quantified from SEM observations (Fig. 7). Filopodia extended furthest on smooth surfaces, reaching 14.62 ± 5.00 μm on ultrafine-grained surfaces and 13.64 ± 6.46 μm on coarse-grained surfaces vs. 3.88 ± 1.37 μm on fine-porous surfaces and 2.89 ± 2.11 μm on coarse-porous surfaces. A similar trend in cell spreading area was observed (Fig. 7B), i.e., much smaller spreading areas on porous surfaces. On this basis, Fig. 8 exhibits representative observations of the cross sections of cells grown on porous surfaces, revealing strong interfacial connections between the cells and the porous surfaces.

Fig. 9 shows representative confocal images for vinculin, actin and nuclei of osteoblasts on each type of surfaces after 8 days of culturing. In general, actin cytoskeletal stress fibres were well developed and vinculins were found distributed on the leading edges of cells as well as at the centre of cells on all the substrate surfaces. Compared to the round cell shapes after culturing for 1 day (Fig. 5E and 5G), cells became less circular or more elongated on fine-porous and coarse-porous surfaces after extending culturing period to 8 days (Fig. 9). In addition, cells on fine-porous and coarse-porous surfaces were noticeably elongated (elongation ratio ~ 3) compared to those on coarse-grained and ultrafine-grained surfaces (elongation ratio < 2) (Fig. 10A). To identify how grain sizes and pore features influence the formation of focal adhesions (FAs), the lengths of FAs were quantified using *Image J*, as shown in Fig. 10B. Cells on fine-porous surfaces were featured by the largest FAs with the average length of 2.50 ± 1.60 μm, followed by coarse-porous surfaces (2.23 ± 1.48 μm), ultrafine-grained surfaces (2.07 ± 0.87 μm) and coarse-grained surfaces (2.05 ± 0.88 μm). In addition, a higher proportion of large and mature FAs (the length ≥ 5 μm) were present on the fine-porous (6.16%) and coarse-porous (6.00%) surfaces than on the coarse-grained (2.89%) and ultrafine-grained (1.84%) surfaces.

Cell number and differentiation

Fig. 11A shows the number of adhered cells on each substrate surface after culturing for 8 days. Both fine-porous and coarse-porous surfaces were more effective in enhancing cell growth than ultrafine-grained surfaces. Furthermore, the normalised ALP activity, which refers to the ALP activity with respect to the protein content, showed clear differences (Fig. 11B). The ALP activity was measured in the absence of any osteogenic medium and represented the level of osteogenic capacity. Coarse-porous surfaces displayed the highest intracellular ALP activity, followed by coarse-grained surfaces, while fine-porous and ultrafine-grained surfaces resulted in low ALP activity. Reducing grain size from 400 μm (coarse-grained) to 100 nm (ultrafine-grained) thus failed to enhance the ALP activity. Rather, it led to the lowest ALP activity. A statistical difference

(p=0.03) was observed in ALP activity between coarse-porous and ultrafine-grained substrates, while no statistical difference (p>0.05) was observed between all other groups.

DISCUSSION

It is evident from the aforementioned comparative study that osteoblasts responded differently to Ti-20Mo surfaces featured with ultrafine grains (submicron) and submicron interconnected pores including cell morphology, adhesion, number and the production of ALP. The effects of ultrafine grains and submicron interconnected pores will be further evaluated below with respect to cell response to surface wettability and length scales of the topographical features.

Surface wettability is one of the decisive factors that dictate the adherence of proteins on an implant surface and thereby affect cell attachment in the early stages [48]. Hydrophilic surfaces often enhance initial cell spreading and osteoblastic differentiation of mesenchymal stem cells [49, 50]. In this study, the water contact angles were found to be similar (58.23 ± 6.28° vs. 61.66 ± 7.76°) for ultrafine-grained and coarse-grained smooth surfaces of Ti-20Mo. Estrin et al. reported similar observations for ultrafine- and coarse-grained smooth surfaces of CP-Ti [23]. However, different observations were made with 316L stainless steel, where ultrafine-grained (grain size: 320 nm; θ=52°) smooth surfaces were found to be more hydrophilic than coarse-grained smooth surfaces (grain size: 22 μm; θ=78°) [51]. This discrepancy might be due to the different properties of the surface oxide films (TiO_2 vs. Cr_2O_3). On the other hand, fine-porous and coarse-porous surfaces of Ti-20Mo were found to be much more hydrophilic than ultrafine-grained and coarse-grained smooth surfaces of Ti-20Mo. This can be attributed to capillary-driven water penetration into the surface pores [52]. It was reported that increasing pore diameter from 85 nm to 400 nm converted the nanoporous alumina surface from hydrophilic (θ=70°) to hydrophobic (θ=132°) [52]. This is consistent with our observations shown in Fig. 4, where increasing average pore size from 155 nm to 350 nm increased the water contact angle from 28° to 39°. In addition, the ratio of pore depth-to-diameter can also affect the infiltration of water into the pores, which involves expelling the

residual gas deep in the interconnected pores [52]. In that regard, deep pores are not always preferred for maximising surface wettability.

Filopodia, which are normally located at the leading edges of cells, are responsible for sensing favourable microenvironments (e.g., suitable proteins) for cells to adhere to [53, 54]. The locations of such microenvironments determine both the direction and distance of subsequent cell migration, which, in turn, involve rearrangement of the cytoskeletons [53, 54]. As shown in Fig. 6, osteoblasts sensed and interacted with pores as small as about 150 nm, and some filopodia eventually grew into them, equivalent to being anchored there. It has been suggested that nutrients and proteins that reside in such pores can attract filopodia to extend into the pores [55]. Consequently, the need for filopodia to sense suitable proteins that exist laterally on the porous surfaces was reduced, and this can explain the reduction in filopodia length on porous surfaces observed in this study (Fig. 5 F, Fig. 5H, Fig. 7A). Zhu et al. reported that both submicron (500 nm) and micron (2 μm) pores were capable of anchoring filopodia, benefiting subsequent cell attachment [56]. Previous studies indicated that submicron pores (~263 nm) were more efficient in facilitating filopodia penetration than nanopores (76 nm) [57, 58] as they were comparable in size to filopodia (100-300 nm) [21]. In this regard, the pore size is important and should be controlled to mimic the length scale of the filopodia for easy detection. This shows the complexity in topographical design of biofunctional surfaces.

In the present work, after culturing for 1 day, osteoblasts adapted themselves to both fine-porous and coarse-porous surfaces and displayed round morphology with limited spreading (Fig. 5 E-H and Fig. 7B). This finding is consistent with a number of studies showing that no matter what cell types were used (human osteoblasts [59], SaoS-2 cells [56], rat mesenchymal stem cells (rMSCs) [60] and human dental pulp stem cells [61]), cell spreading has been hindered by topographical features on concave surfaces such as nanoscaled (30-60 nm), submicron (120-500 nm) and micron (2 μm) pores/pits. The reduced cell spreading on porous surfaces can be attributed to the influence of pore depth. In the early stages of attachment, cells tend to conform to the pore shape, leaving

cytoskeleton actins in a stressed state [62]. In order to reduce the stress, cells choose to minimise their interfacial contact with the surface, which accordingly reduces cell spreading [62]. As coarse-porous surfaces are deeper than fine-porous surfaces, the cell-surface contact was more restricted. Consequently, cell spreading on coarse-porous surfaces (458.8 ± 235.5 μm^2) was clearly less than that on fine-porous surface (630.2 ± 327.6 μm^2) as shown in Fig. 7B. On the other hand, robust attachments of osteoblasts were found on both fine-porous and coarse-porous surfaces (Fig. 8), suggesting close cell interactions with pores through ingrowth. This is an indicator of strong cell adhesion and fixation to the porous surface and is thus highly desired for long-time implantation [63]. In contrast, the absence of stable anchoring sites on a smooth surface appears to facilitate cells spreading.

FAs link intracellular actin cytoskeleton structures to extracellular matrices (ECM), transduce signals to the nuclei and regulate the expressions or pathways of related genes [64]. According to Fig.10B, a higher proportion of large FAs (marked with vinculin proteins) were present on both fine-porous and coarse-porous surfaces than on ultrafine-grained and coarse-grained smooth surfaces, revealing that rougher surfaces tend to facilitate the formation of FAs. Gentile et al. proposed that the tips of the protrusions on rough surfaces acted as initial sites for the contact of cells [65]. Progressively, the cell membrane extended into the vicinity of the protrusion tips and finally wrapped around the tips to promote the formation of FAs [65]. Thus, in the present study, the size and geometry of the ligaments of the interconnected porous surface structure play a crucial role in providing a large number of sites for the formation of FAs.

Both cell growth and osteogenic capacity are important for long-term osseointegration. In this study, a substantial increase in grain boundaries was found to be much less effective for cell growth than having a submicron porous surface. Oh et al. reported that enhanced cell growth was correlated to higher wettability and larger area on the surface [66]. As shown in Fig. 4 and Table 4, owing to their porous characteristics, the surface energies of both fine-porous and coarse-porous surfaces were twice that of the dense coarse-grained and ultrafine-grained smooth surfaces. An

increased number of cells adhered to both fine-porous and coarse-porous surfaces can thus be ascribed to the greatly improved wettability and increased surface area. Bello et al. showed that larger FAs were associated with a higher number of cells on nanoporous CP-Ti surfaces (pore diameter: 20 ± 5 nm) [67]. In addition, at the initial stage of cell culturing, a smaller cell spreading area on porous surfaces allows more cells to anchor on porous surfaces than dense coarse-grained and ultrafine-grained surfaces [60].

As no osteogenic medium such as dexamethasone, ascorbic acid, vitamin D_3 or β-glycerophosphate was introduced to the culture medium, the observed ALP activity was solely determined by the surface topography [66, 68], and this, in turn, affected cell morphology. As shown in Fig. 11B, coarse-porous surfaces produced significantly enhanced intracellular ALP activity compared with ultrafine-grained smooth surfaces. The enhanced ALP activity was found relevant to cell morphology. Oh et al. demonstrated that highly elongated MSCs on 100-nm diameter nanotubes led to increased osteogenic gene expressions [66]. The noticeable cell elongation on the coarse-porous surfaces was probably linked to the enhanced ALP activity (Fig. 10A). In addition, Biggs et al. demonstrated that the enhanced formation of FAs upregulated intracellular ERK/MAPK signalling, which ultimately promoted osteoblastic differentiation in HOBs [59]. Thus, the presence of high proportion of large FAs could lead to the enhanced ALP activity on the coarse-porous surfaces (Fig. 11B). Besides, in general, water molecules and proteins adhere to the implant surface prior to cells interacting with an implant [69]. The adsorption of proteins to a surface is determined by the surface features and rougher surfaces tend to adsorb more protein aggregates than flat surfaces [69]. As one of ECM-located proteins, fibronectin (FN) plays an important role in stimulating osteogenic differentiation and bone formation [70]. Coarse-porous surfaces provided more ligament areas than fine-porous surfaces for FN adsorption and also for integrins to cluster on them [62]. Neither ultrafine-grained nor coarse-grained smooth surfaces provide such surface areas. As a result, coarse-porous surfaces offered the most favourable *in vitro* microenvironment for osteoblasts. Such an optimum topography may benefit osseointegration *in vivo*. However, further *in vivo* studies are needed to

determine the final implant functionality [71]. An effective design is to introduce a coarse-porous surface layer into an ultrafine-grained titanium implant where the latter offers high strength for lightweighting without increasing modulus while the former ensures desired cell responses.

CONCLUSIONS

The effect of surface topographical features on *in vitro* cell responses including cell morphology, adhesion, growth and differentiation has been studied by comparing coarse-grained (grain size: 500 μm), ultrafine-grained (grain size: 100 nm), coarse-porous (pore size: 350 nm) and fine-porous (pore size: 155 nm) surfaces of Ti-20Mo alloy. The following conclusions can be drawn:

1) The coarse-porous surface offered the optimum topographical environment for osteoblasts.
2) After culturing for 1 day, both the coarse-porous and fine-porous surfaces restrained the extension of filopodia and the spreading of cells due to the anchoring effect introduced by the submicron pores.
3) With increasing culturing period to 8 days, both coarse-porous and fine-porous surfaces enhanced the formation of large and mature focal adhesions compared with either coarse-grained or ultrafine-grained surfaces, which resulted in good adhesion of osteoblasts to the porous surfaces of Ti-20Mo.
4) Substantial grain refinement from 400 μm to 100 nm exerted limited influence on filopodia extension and cell growth.
5) Both coarse-porous and fine-porous surfaces exhibited significant surface wettability compared with coarse-grained and ultrafine-grained surfaces. However, surface wettability does not completely define the biofunctionality of a porous metallic surface. Rather, pore features (size and depth) were found to play an important role in regulating cell responses.

These findings collectively suggest that osteoblasts are more responsive to submicron pores (pore size: 155 or 350 nm) than submicron grains. In addition, cells can discern the difference in

pore size and depth and respond differently. Therefore, controlling porous features of an orthopaedic titanium implant is essential to achieve desired functionality for rapid osseointegration.

ACKNOWLEDGMENT

N. Gui acknowledges the support from China Scholarship Council (CSC). R. Shukla acknowledges research support of Ian Potter Foundation and Maxwell Eagle Endowment. Dr. Matthew Field is thanked for significant assistance in microscopic analysis. Dr. Chaitali Dekiwadia is thanked for assistance in solution preparation for cell morphology observation using SEM. Assoc. Prof. Yuncang Li is thanked for training on an optical tensiometer. This work was supported by the Australian Research Council (ARC) through ARC LP140100607.

REFERENCES

1. Wang X, Xu S, Zhou S, Xu W, Leary M, Choong P, Qian M, Brandt M, Xie YM. Topological Design and Additive Manufacturing of Porous Metals for Bone Scaffolds and Orthopaedic Implants: A Review. Biomaterials 2016; 83 127-141.

2. Xie F, He X, Cao S, Mei M, Qu X. Influence of pore characteristics on microstructure, mechanical properties and corrosion resistance of selective laser sintered porous Ti–Mo alloys for biomedical applications. Electrochimica Acta 2013; 105 121-129.

3. Zhao X, Niinomi M, Nakai M, Hieda J. Beta type Ti–Mo alloys with changeable Young's modulus for spinal fixation applications. Acta biomaterialia 2012; 8(5): 1990-1997.

4. Polmear I, StJohn D, Nie J-F, Qian M. Light alloys: metallurgy of the light metals, Butterworth-Heinemann2017.

5. Bania PJ. Beta titanium alloys and their role in the titanium industry. JOM Journal of the Minerals Metals and Materials Society 1994; 46(7): 16-19.

6. Oliveira N, Guastaldi AC. Electrochemical stability and corrosion resistance of Ti–Mo alloys for biomedical applications. Acta Biomaterialia 2009; 5(1): 399-405.

7. Rajagopalan K. Molybdenum: an essential trace element in human nutrition. Annual review of nutrition 1988; 8(1): 401-427.

8. Bolat G, Mareci D, Chelariu R, Izquierdo J, González S, Souto R. Investigation of the electrochemical behaviour of TiMo alloys in simulated physiological solutions. Electrochimica Acta 2013; 113 470-480.

9. Oliveira NTC, Aleixo G, Caram R, Guastaldi AC. Development of Ti–Mo alloys for biomedical applications: Microstructure and electrochemical characterization. Materials Science and Engineering: A 2007; 452 727-731.

10. Almeida A, Gupta D, Loable C, Vilar R. Laser-assisted synthesis of Ti–Mo alloys for biomedical applications. Materials Science and Engineering: C 2012; 32(5): 1190-1195.

11. Jiin-Huey Chern Lin C-PJ, Wen-Fu Ho. Biocompatible low modulus titanium alloy for medical implant, United States, 2002.

12. Sjöström T, Lalev G, Mansell JP, Su B. Initial attachment and spreading of MG63 cells on nanopatterned titanium surfaces via through-mask anodization. Applied Surface Science 2011; 257(10): 4552-4558.

13. Jablokov VR, Nutt MJ, Richelsoph ME, Freese HL. The application of Ti-15Mo beta titanium alloy in high strength structural orthopaedic applications. Journal of ASTM International 2005; 2(8): 1-18.

14. Bolat G, Izquierdo J, Gloriant T, Chelariu R, Mareci D, Souto R. Investigation of processing effects on the corrosion resistance of Ti20Mo alloy in saline solutions. Corrosion Science 2015; 98 170-179.

15. Xu W, Wu X, Stoica M, Calin M, Kühn U, Eckert J, Xia K. On the formation of an ultrafine-duplex structure facilitated by severe shear deformation in a Ti–20Mo β-type titanium alloy. Acta Materialia 2012; 60(13): 5067-5078.

16. Xu W, Edwards DP, Wu X, Stoica M, Calin M, Kühn U, Eckert J, Xia K. Promoting nano/ultrafine-duplex structure via accelerated α precipitation in a β-type titanium alloy severely deformed by high-pressure torsion. Scripta Materialia 2013; 68(1): 67-70.

17. Takemoto Y, Shimizu I, Sakakibara A, Hida M, Mantani Y. Tensile Behavior and Cold Workability of Ti-Mo Alloys. MATERIALS TRANSACTIONS 2004; 45(5): 1571-1576.

18. Gittens RA, Olivares-Navarrete R, Schwartz Z, Boyan BD. Implant osseointegration and the role of microroughness and nanostructures: Lessons for spine implants. Acta Biomaterialia 2014; 10(8): 3363-3371.

19. Williams DF. Biocompatibility Pathways; Biomaterials-Induced Sterile Inflammation, Mechanotransduction and Principles of Biocompatibility Control. ACS Biomaterials Science & Engineering 2016.

20. Metavarayuth K, Sitasuwan P, Zhao X, Lin Y, Wang Q. Influence of surface topographical cues on the differentiation of mesenchymal stem cells in vitro. ACS Biomaterials Science & Engineering 2016; 2(2): 142-151.

21. Nguyen AT, Sathe SR, Yim EK. From nano to micro: topographical scale and its impact on cell adhesion, morphology and contact guidance. Journal of Physics: Condensed Matter 2016; 28(18): 183001.

22. Huang R, Lu S, Han Y. Role of grain size in the regulation of osteoblast response to Ti-25Nb-3Mo-3Zr-2Sn alloy. Colloids and Surfaces B: Biointerfaces 2013; 111 232-241.

23. Estrin Y, Ivanova EP, Michalska A, Truong VK, Lapovok R, Boyd R. Accelerated stem cell attachment to ultrafine grained titanium. Acta biomaterialia 2011; 7(2): 900-906.

24. Misra R, Thein-Han W, Pesacreta T, Hasenstein K, Somani M, Karjalainen L. Cellular response of preosteoblasts to nanograined/ultrafine-grained structures. Acta biomaterialia 2009; 5(5): 1455-1467.

25. Saldaña L, Méndez-Vilas A, Jiang L, Multigner M, González-Carrasco JL, Pérez-Prado MT, González-Martín ML, Munuera L, Vilaboa N. In vitro biocompatibility of an ultrafine grained zirconium. Biomaterials 2007; 28(30): 4343-4354.

26. Yilmazer H, Şen M, Niinomi M, Nakai M, Huihong L, Cho K, Todaka Y, Shiku H, Matsue T. Developing biomedical nano-grained β-type titanium alloys using high pressure torsion for improved cell adherence. RSC Advances 2016; 6(9): 7426-7430.

27. Valiev R, Estrin Y, Horita Z, Langdon T, Zehetbauer M, Zhu Y. Fundamentals of superior properties in bulk nanoSPD materials. Materials Research Letters 2016; 4(1): 1-21.

28. Polyakov AV, Dluhoš L, Dyakonov GS, Raab GI, Valiev RZ. Recent advances in processing and application of nanostructured titanium for dental implants. Advanced Engineering Materials 2015; 17(12): 1869-1875.

29. Weller M, Diehl J, Schaefer HE. Shear modulus and internal friction in nanometre-sized polycrystalline palladium. Philosophical Magazine A 1991; 63(3): 527-533.

30. Fougere GE, Riester L, Ferber M, Weertman JR, Siegel RW. Young's modulus of nanocrystalline Fe measured by nanoindentation. Materials Science and Engineering: A 1995; 204(1): 1-6.

31. Sanders PG, Eastman JA, Weertman JR. Elastic and tensile behavior of nanocrystalline copper and palladium. Acta Materialia 1997; 45(10): 4019-4025.

32. Giallonardo JD, Erb U, Aust KT, Palumbo G. The influence of grain size and texture on the Young's modulus of nanocrystalline nickel and nickel–iron alloys. Philosophical Magazine 2011; 91(36): 4594-4605.

33. Gatina S, Semenova I, Leuthold J, Valiev R. Nanostructuring and Phase Transformations in the β-Alloy Ti-15Mo during High-Pressure Torsion. Advanced Engineering Materials 2015; 17(12): 1742-1747.

34. Greiner C, Oppenheimer SM, Dunand DC. High strength, low stiffness, porous NiTi with superelastic properties. Acta Biomaterialia 2005; 1(6): 705-716.

35. Liu X, Wu S, Yeung KWK, Chan YL, Hu T, Xu Z, Liu X, Chung JCY, Cheung KMC, Chu PK. Relationship between osseointegration and superelastic biomechanics in porous NiTi scaffolds. Biomaterials 2011; 32(2): 330-338.

36. Kutty MG, De A, Bhaduri SB, Yaghoubi A. Microwave-assisted fabrication of titanium implants with controlled surface topography for rapid bone healing. ACS applied materials & interfaces 2014; 6(16): 13587-13593.

37. Wang XJ, Li YC, Hodgson PD, Wen C. Biomimetic Modification of Porous TiNbZr Alloy Scaffold for Bone Tissue Engineering. Tissue Eng. Part A 2010; 16(1): 309-316.

38. Hollister SJ. Porous scaffold design for tissue engineering. Nature Materials 2005; 4(7): 518-524.

39. Wu S, Liu X, Yeung KW, Liu C, Yang X. Biomimetic porous scaffolds for bone tissue engineering. Materials Science and Engineering: R: Reports 2014; 80 1-36.

40. McClay DR. The Role of Thin Filopodia in Motility and Morphogenesis. Experimental Cell Research 1999; 253(2): 296-301.

41. Zhilyaev AP, Langdon TG. Using high-pressure torsion for metal processing: Fundamentals and applications. Progress in Materials Science 2008; 53(6): 893-979.

42. Carré A. Polar interactions at liquid/polymer interfaces. Journal of Adhesion Science and Technology 2007; 21(10): 961-981.

43. Abràmoff MD, Magalhães PJ, Ram SJ. Image processing with ImageJ. Biophotonics international 2004; 11(7): 36-42.

44. Horzum U, Ozdil B, Pesen-Okvur D. Step-by-step quantitative analysis of focal adhesions. MethodsX 2014; 1 56-59.

45. Biggs MJ, Richards R, Gadegaard N, Wilkinson C, Dalby M. Regulation of implant surface cell adhesion: Characterization and quantification of S ‐ phase primary osteoblast adhesions on biomimetic nanoscale substrates. Journal of Orthopaedic Research 2007; 25(2): 273-282.

46. Yilmazer H, Niinomi M, Cho K, Nakai M, Lui H, Todaka Y, Dikici B, Şen M, Shiku H, Matsue T. Mechanical and Surface Functionalities of Nanostructured β–Type Titanium Alloys Through Severe Plastic Deformation, Proceedings of the 13th World Conference on Titanium, John Wiley & Sons, Inc.2016, pp. 1761-1766.

47. Zhang Q, Dong H, Li Y, Zhu Y, Zeng L, Gao H, Yuan B, Chen X, Mao C. Microgrooved Polymer Substrates Promote Collective Cell Migration To Accelerate Fracture Healing in an in Vitro Model. ACS applied materials & interfaces 2015; 7(41): 23336-23345.

48. Gittens RA, Scheideler L, Rupp F, Hyzy SL, Geis-Gerstorfer J, Schwartz Z, Boyan BD. A review on the wettability of dental implant surfaces II: Biological and clinical aspects. Acta Biomaterialia 2014; 10(7): 2907-2918.

49. Lim JY, Taylor AF, Li Z, Vogler EA, Donahue HJ. Integrin expression and osteopontin regulation in human fetal osteoblastic cells mediated by substratum surface characteristics. Tissue engineering 2005; 11(1-2): 19-29.

50. Olivares-Navarrete R, Hyzy SL, Hutton DL, Erdman CP, Wieland M, Boyan BD, Schwartz Z. Direct and indirect effects of microstructured titanium substrates on the induction of mesenchymal stem cell differentiation towards the osteoblast lineage. Biomaterials 2010; 31(10): 2728-2735.

51. Misra RDK, Nune C, Pesacreta TC, Somani MC, Karjalainen LP. Understanding the impact of grain structure in austenitic stainless steel from a nanograined regime to a coarse-grained regime on osteoblast functions using a novel metal deformation–annealing sequence. Acta Biomaterialia 2013; 9(4): 6245-6258.

52. Ran C, Ding G, Liu W, Deng Y, Hou W. Wetting on Nanoporous Alumina Surface: Transition between Wenzel and Cassie States Controlled by Surface Structure. Langmuir 2008; 24(18): 9952-9955.

53. Dalby MJ, Gadegaard N, Riehle MO, Wilkinson CDW, Curtis ASG. Investigating filopodia sensing using arrays of defined nano-pits down to 35 nm diameter in size. The International Journal of Biochemistry & Cell Biology 2004; 36(10): 2005-2015.

54. Mattila PK, Lappalainen P. Filopodia: molecular architecture and cellular functions. Nature reviews Molecular cell biology 2008; 9(6): 446-454.

55. Hoess A, Thormann A, Friedmann A, Heilmann A. Self‐supporting nanoporous alumina membranes as substrates for hepatic cell cultures. Journal of biomedical materials research Part A 2012; 100(9): 2230-2238.

56. Zhu X, Chen J, Scheideler L, Altebaeumer T, Geis-Gerstorfer J, Kern D. Cellular reactions of osteoblasts to micron-and submicron-scale porous structures of titanium surfaces. Cells Tissues Organs 2004; 178(1): 13-22.

57. Hoess A, Teuscher N, Thormann A, Aurich H, Heilmann A. Cultivation of hepatoma cell line HepG2 on nanoporous aluminum oxide membranes. Acta biomaterialia 2007; 3(1): 43-50.

58. Friedmann A, Hoess A, Cismak A, Heilmann A. Investigation of cell–substrate interactions by focused ion beam preparation and scanning electron microscopy. Acta biomaterialia 2011; 7(6): 2499-2507.

59. Biggs MJ, Richards RG, Gadegaard N, Wilkinson CD, Oreffo RO, Dalby MJ. The use of nanoscale topography to modulate the dynamics of adhesion formation in primary osteoblasts and ERK/MAPK signalling in STRO-1+ enriched skeletal stem cells. Biomaterials 2009; 30(28): 5094-5103.

60. Wang PY, Clements LR, Thissen H, Jane A, Tsai WB, Voelcker NH. Screening mesenchymal stem cell attachment and differentiation on porous silicon gradients. Advanced Functional Materials 2012; 22(16): 3414-3423.

61. Karakeçili A, Messina GML, Yurtsever MÇ, Gümüşderelioğlu M, Marletta G. Impact of selective fibronectin nanoconfinement on human dental pulp stem cells. Colloids and Surfaces B: Biointerfaces 2014; 123 39-48.

62. Kunzler TP, Huwiler C, Drobek T, Vörös J, Spencer ND. Systematic study of osteoblast response to nanotopography by means of nanoparticle-density gradients. Biomaterials 2007; 28(33): 5000-5006.

63. Blakeney BA, Tambralli A, Anderson JM, Andukuri A, Lim D-J, Dean DR, Jun H-W. Cell infiltration and growth in a low density, uncompressed three-dimensional electrospun nanofibrous scaffold. Biomaterials 2011; 32(6): 1583-1590.

64. Anselme K, Davidson P, Popa AM, Giazzon M, Liley M, Ploux L. The interaction of cells and bacteria with surfaces structured at the nanometre scale. Acta Biomaterialia 2010; 6(10): 3824-3846.

65. Gentile F, Tirinato L, Battista E, Causa F, Liberale C, Di Fabrizio EM, Decuzzi P. Cells preferentially grow on rough substrates. Biomaterials 2010; 31(28): 7205-7212.

66. Oh S, Brammer KS, Li YJ, Teng D, Engler AJ, Chien S, Jin S. Stem cell fate dictated solely by altered nanotube dimension. Proceedings of the National Academy of Sciences 2009; 106(7): 2130-2135.

67. Guadarrama Bello D, Fouillen A, Badia A, Nanci A. A nanoporous titanium surface promotes the maturation of focal adhesions and formation of filopodia with distinctive nanoscale protrusions by osteogenic cells. Acta Biomaterialia 2017; 60 339-349.

68. Wilkinson A, Hewitt RN, McNamara LE, McCloy D, Meek RD, Dalby MJ. Biomimetic microtopography to enhance osteogenesis in vitro. Acta biomaterialia 2011; 7(7): 2919-2925.

69. Anselme K. Osteoblast adhesion on biomaterials. Biomaterials 2000; 21(7): 667-681.

70. Globus R, Doty S, Lull J, Holmuhamedov E, Humphries M, Damsky C. Fibronectin is a survival factor for differentiated osteoblasts. Journal of Cell Science 1998; 111(10): 1385-1393.

71. Gui N, Xu W, Myers DE, Shukla R, Tang HP, Qian M. The effect of ordered and partially ordered surface topography on bone cell responses: a review. Biomaterials Science 2018; 6(2): 250-264.

Figure legends

Fig. 1. (A) SEM micrograph of the coarse-grained substrate with an average grain size of 500 μm, (B) TEM bright-field micrograph of the ultrafine-grained substrate with an average grain size of 100 nm. Yellow dashed line indicates the grain boundary in the ultrafine-grained substrate.

Fig. 2. XRD profiles of the coarse-grained, ultrafine-grained, fine-porous and coarse-porous surfaces of Ti-20Mo.

Fig. 3. Topography analyses of Ti-20Mo porous surfaces. SEM images of fine-porous surfaces at (A) low and (C) high magnifications; (B) AFM images and (D) pore size distribution of fine-porous surfaces. SEM images of coarse-porous surfaces at (E) low and (G) high magnifications; (F) AFM images and (H) pore size distribution of coarse-porous surfaces. See Table 1 for their S_a and S_q values.

Fig. 4. Water contact angle of different Ti-20Mo surfaces and water droplet morphology (mean ± SD, * $p < 0.05$ vs. coarse-grained surfaces, # $p < 0.05$ vs. ultrafine-grained surfaces, & $p < 0.05$ vs. fine-porous surfaces).

Fig. 5. SEM images of osteoblasts grown on various Ti-20Mo surfaces after culturing for 1 day. (A-B): coarse-grained surfaces, (C-D): ultrafine-grained surfaces, (E-F): fine-porous surfaces and (G-H): coarse-porous surfaces. Left column: low-magnification SEM images, right column: high-magnification SEM images. Yellow arrows indicate that filopodia interacted with Ti-20Mo surfaces.

Fig. 6. The interactions between filopodia and pores on the fine-porous surfaces of Ti-20Mo.

Fig. 7. (A): filopodia length and (B): cell spreading area of osteoblasts after culturing for 1 day on different Ti-20Mo surfaces (mean ± SD, *: $p < 0.05$ vs. coarse-grained surfaces, **: $p < 0.001$ vs.

coarse-grained surfaces, #: $p < 0.05$ vs. ultrafine-grained surfaces, ##: $p < 0.001$ vs. ultrafine-grained surfaces, &: $p < 0.05$ vs. fine-porous surfaces).

Fig. 8. Cross section images of osteoblasts grown on porous surfaces of Ti-20Mo substrates after culturing for 1 day: (A) fine-porous and (B) coarse-porous surfaces.

Fig. 9. Confocal microscopy images of osteoblasts grown on all substrates after culturing for 8 days. Cells were stained with phalloidin (green) for actin filaments, Hoechst (blue) for nuclei, anti-vinculin (red) for focal adhesions.

Fig. 10. (A): elongation ratio (cell long axis/short axis) and (B): the length distribution of focal adhesions on various Ti-20Mo substrates after culturing for 8 days (mean ± SD, *: $p < 0.05$ vs. coarse-grained surfaces, #: $p < 0.05$ vs. ultrafine-grained surfaces).

Fig. 11. (A): total cell number and (B): ALP activity normalised to protein content of osteoblasts cultured on different Ti-20Mo surfaces for 8 days. (mean ± SD, * $p < 0.05$ vs. coarse-grained surfaces, #: $p < 0.05$ vs. ultrafine-grained surfaces).

Table 1 Preparation methods, microstructural and surface features of Ti-20Mo alloy substrates.

Substrate	Preparation methods						Microstructural features [16]	Surface features
	Solution treated at 1000°C for 48 h	HPT	Aging at 550 °C		Polishing	Acid etching		
			0 min	60 min				
Coarse grained	√				√		Coarse β grains ~ 500 μm	Flat: low fraction of grain boundaries (GBs)
Ultrafine grained	√	√			√		Ultrafine β grains ~ 100 nm	Flat: high fraction of GBs
Fine porous	√	√	√		√	√	Mixture of α & β ultrafine grains ~ 100 nm	Interconnected pores
Coarse porous	√	√		√	√	√	Mixture of α & β ultrafine grains ~ 250 nm	Interconnected pores

Table 2 Surface average roughness (S_a) and root mean square roughness (S_q) values of coarse-grained and ultrafine-grained substrates; pore size and the thickness of the porous surface layer for the fine-porous and coarse-porous substrates (For surface roughness, three areas were measured on each sample and each area was measured to be 3 μm × 3 μm).

Substrate	**S_a (nm)**	**S_q (nm)**
Coarse grained	0.64 ± 0.37	1.11 ± 0.61
Ultrafine grained	0.33 ± 0.19	0.72 ± 0.41
	Pore size (nm)	**Thickness of the porous surface layer (nm)**
Fine porous	155 ± 38	950 ± 120
Coarse porous	350 ± 96	1950 ± 250

Table 3 XPS surface composition analysis for the studied Ti-20Mo substrates.

Substrate	**Ti (wt.%)**	**Mo (wt.%)**
Coarse grained	81.81	18.17
Ultrafine grained	81.83	18.17
Fine porous	67.84	32.16
Coarse porous	64.22	35.78

Table 4 Surface free energy of different Ti-20Mo surfaces (mean ± SD, * $p < 0.05$ vs. coarse-grained substrates, # $p < 0.05$ vs. ultrafine-grained substrates).

Substrate	Dispersive component γ^d (mJ/m^2)	Polar component γ^p (mJ/m^2)	Total surface free energy γ (mJ/m^2)
Coarse grained	7.01 ± 1.29	25.71 ± 5.39	32.72 ± 5.69
Ultrafine grained	2.69 ± 1.23*	37. 83 ± 6.97	40.52 ± 6.63
Fine porous	1.21 ± 0.41*	79.10 ± 4.65*#	80.31 ± 2.94*#
Coarse porous	5.40 ± 1.93	73.95 ± 7.15*#	79.35 ± 2.37*#

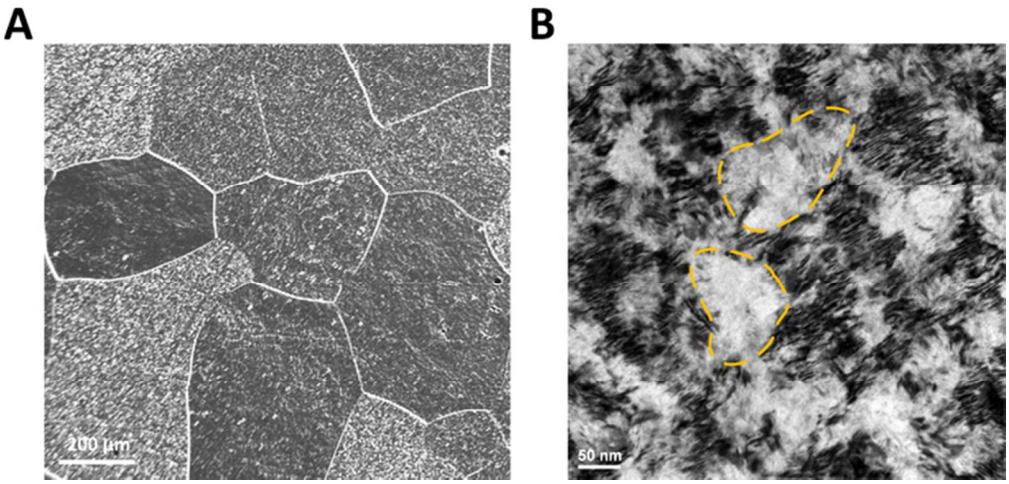

Fig. 1. (A) SEM micrograph of the coarse-grained substrate with an average grain size of 500 µm, (B) TEM bright-field micrograph of the ultrafine-grained substrate with an average grain size of 100 nm. Yellow dashed line indicates the grain boundary in the ultrafine-grained substrate.

62x30mm (300 x 300 DPI)

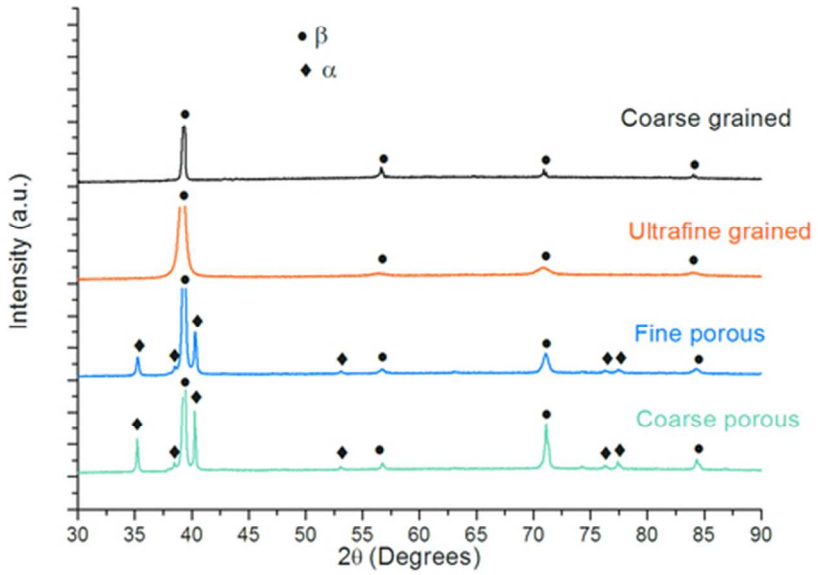

Fig. 2. XRD profiles of the coarse-grained, ultrafine-grained, fine-porous and coarse-porous surfaces of Ti-20Mo.

25x17mm (600 x 600 DPI)

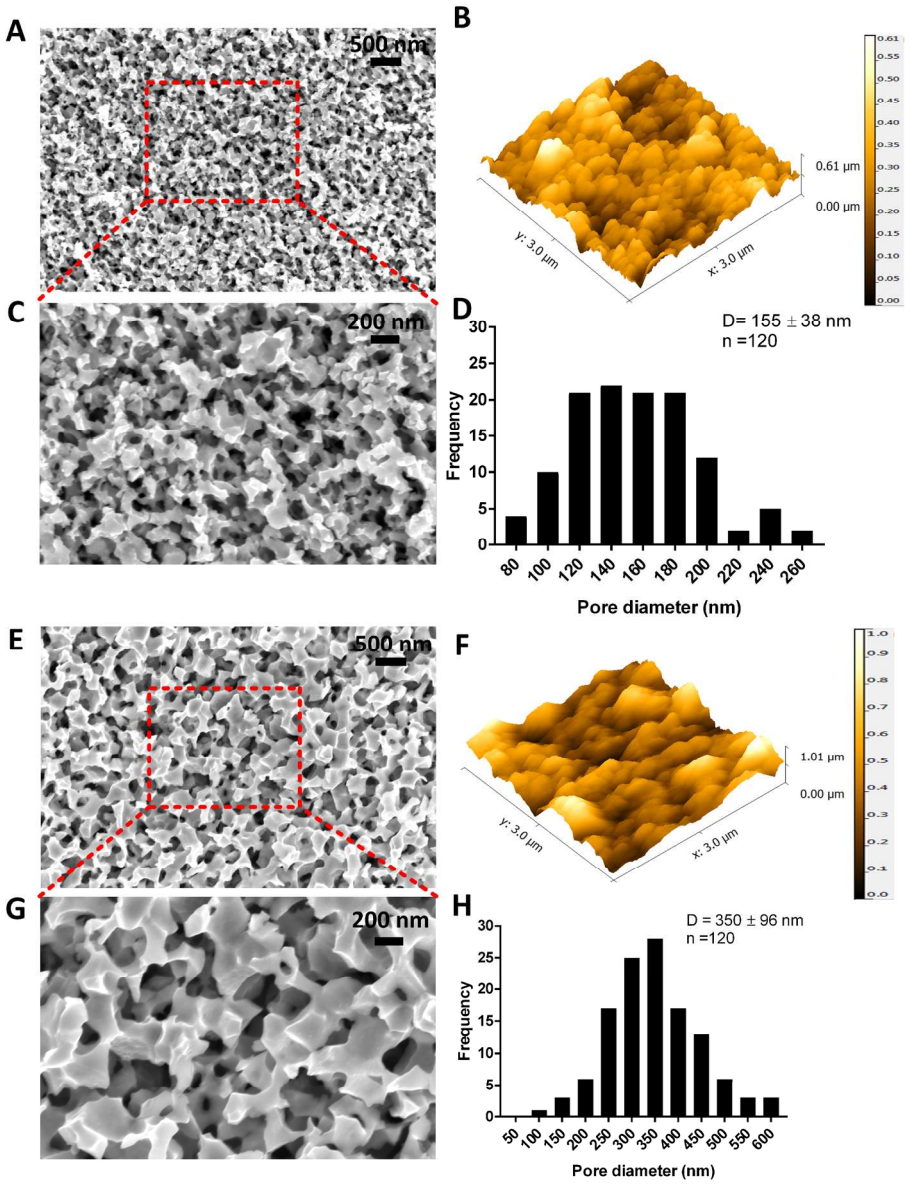

Fig. 3. Topography analyses of Ti-20Mo porous surfaces. SEM images of fine-porous surfaces at (A) low and (C) high magnifications; (B) AFM images and (D) pore size distribution of fine-porous surfaces. SEM images of coarse-porous surfaces at (E) low and (G) high magnifications; (F) AFM images and (H) pore size distribution of coarse-porous surfaces. See Table 1 for their Sa and Sq values.

169x226mm (300 x 300 DPI)

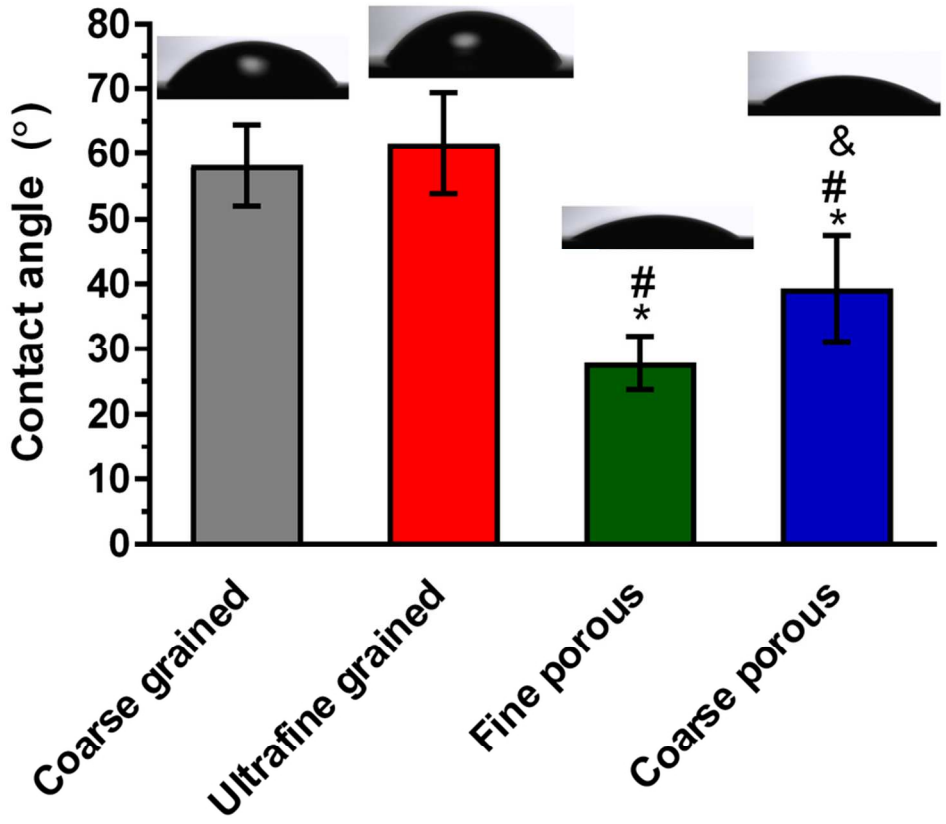

Fig. 4. Water contact angle of different Ti-20Mo surfaces and water droplet morphology (mean ± SD, * $p < 0.05$ vs. coarse-grained surfaces, # $p < 0.05$ vs. ultrafine-grained surfaces, & $p < 0.05$ vs. fine-porous surfaces).

83x74mm (300 x 300 DPI)

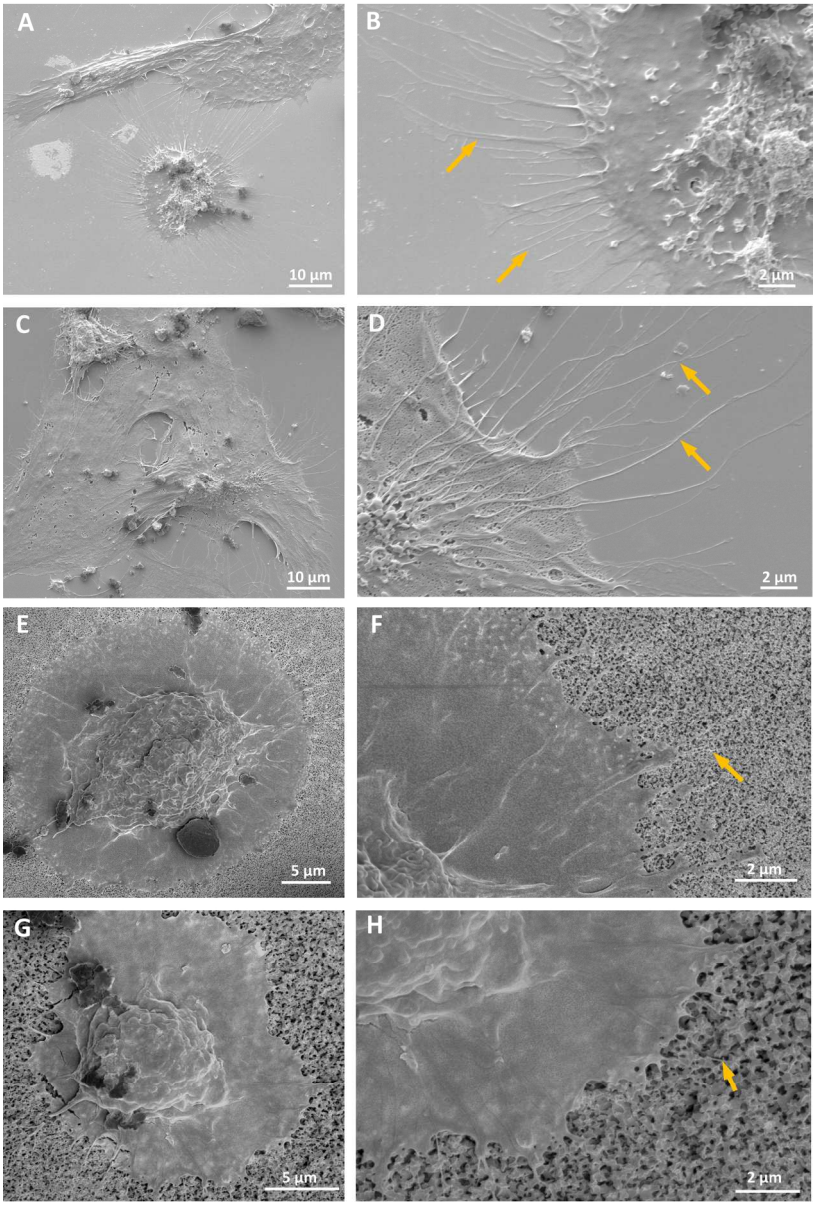

Fig. 5. SEM images of osteoblasts grown on various Ti-20Mo surfaces after culturing for 1 day. (A-B): coarse-grained surfaces, (C-D): ultrafine-grained surfaces, (E-F): fine-porous surfaces and (G-H): coarse-porous surfaces. Left column: low-magnification SEM images, right column: high-magnification SEM images. Yellow arrows indicate that filopodia interacted with Ti-20Mo surfaces.

146x218mm (300 x 300 DPI)

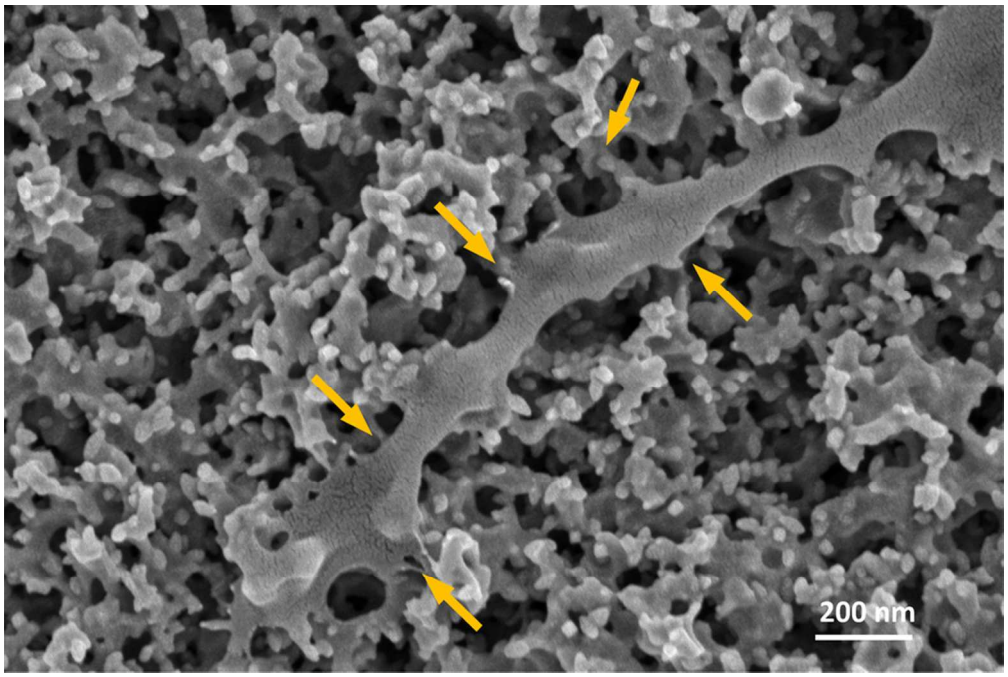

Fig. 6. The interactions between filopodia and pores on the fine-porous surfaces of Ti-20Mo.

84x56mm (300 x 300 DPI)

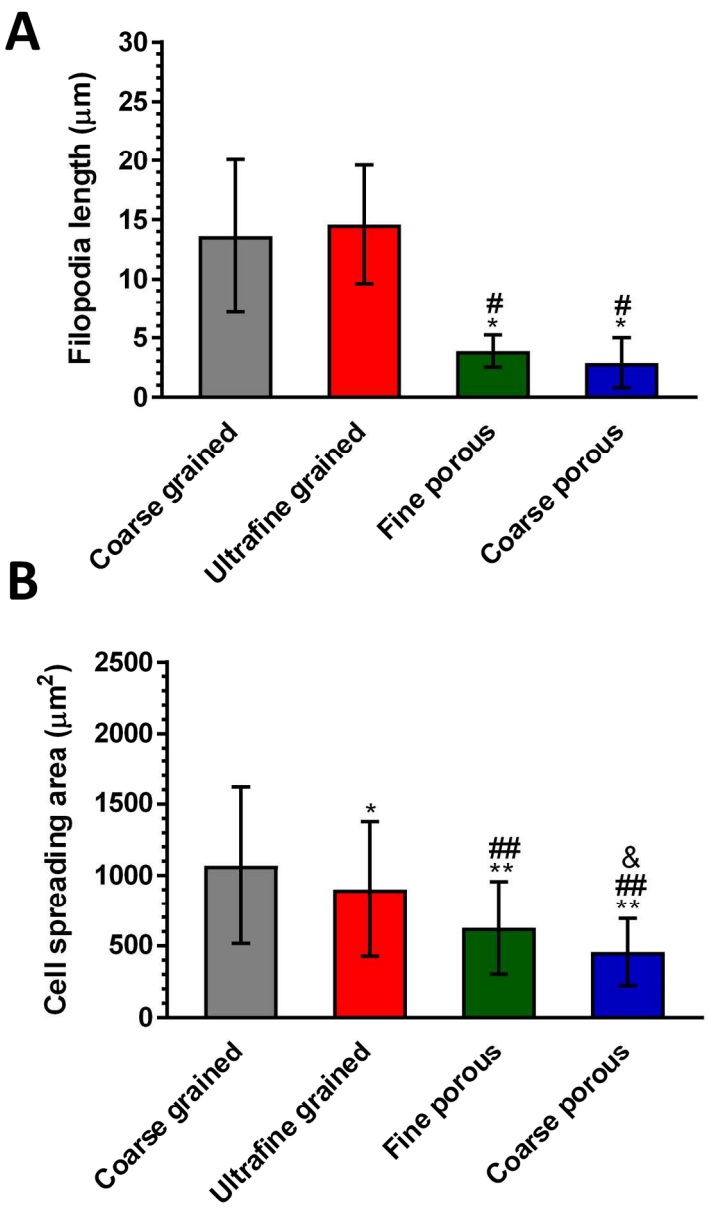

Fig. 7. (A): filopodia length and (B): cell spreading area of osteoblasts after culturing for 1 day on different Ti-20Mo surfaces (mean ± SD, *: $p < 0.05$ vs. coarse-grained surfaces, **: $p < 0.001$ vs. coarse-grained surfaces, #: $p < 0.05$ vs. ultrafine-grained surfaces, ##: $p < 0.001$ vs. ultrafine-grained surfaces, &: $p < 0.05$ vs. fine-porous surfaces).

128x219mm (300 x 300 DPI)

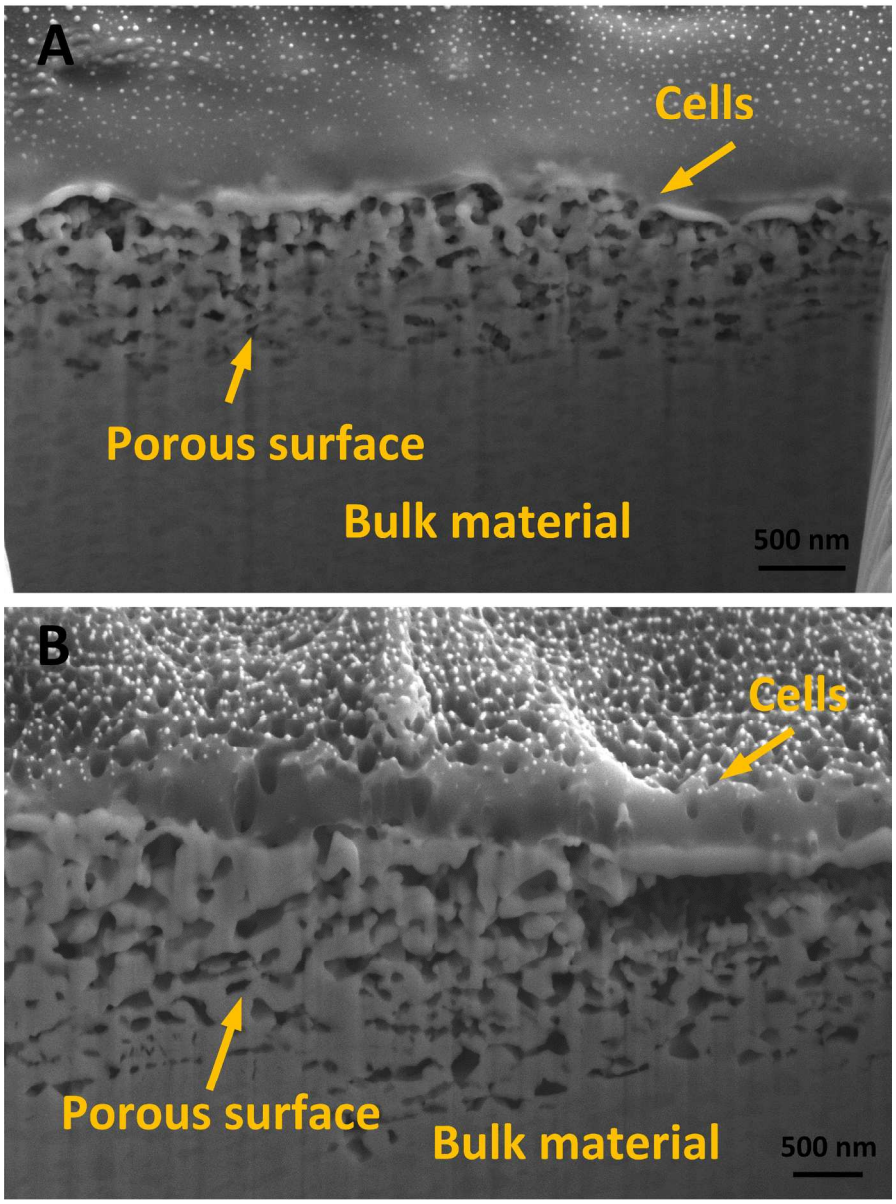

Fig. 8. Cross section images of osteoblasts grown on porous surfaces of Ti-20Mo substrates after culturing for 1 day: (A) fine-porous and (B) coarse-porous surfaces.

171x232mm (300 x 300 DPI)

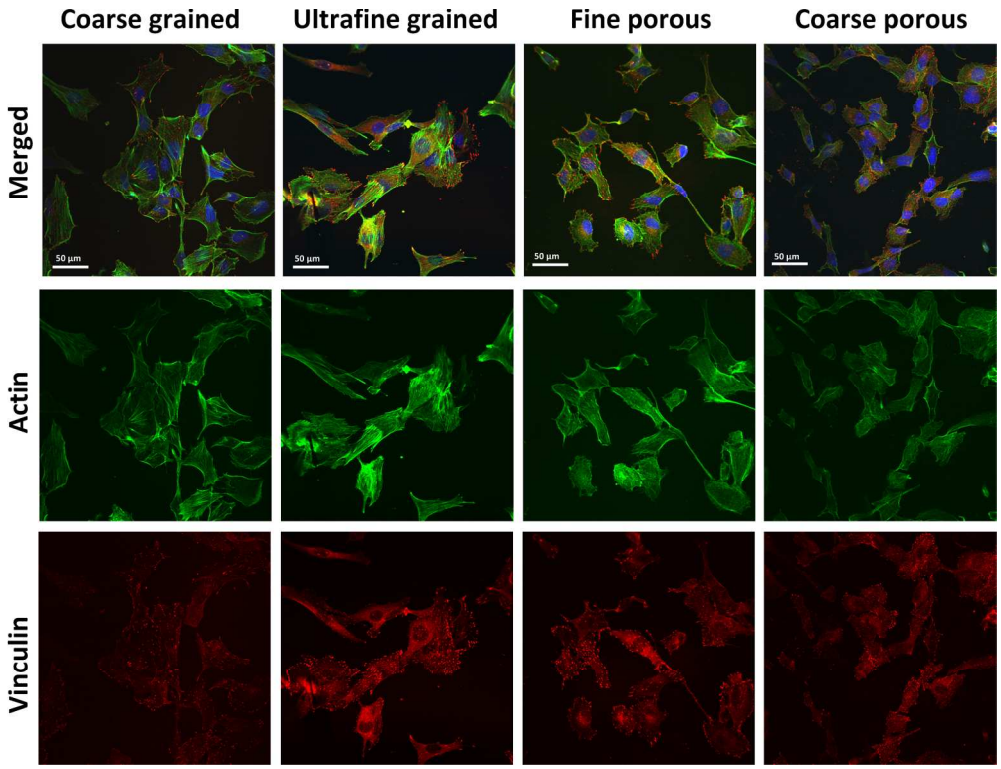

Fig. 9. Confocal microscopy images of osteoblasts grown on all substrates after culturing for 8 days. Cells were stained with phalloidin (green) for actin filaments, Hoechst (blue) for nuclei, anti-vinculin (red) for focal adhesions.

582x439mm (96 x 96 DPI)

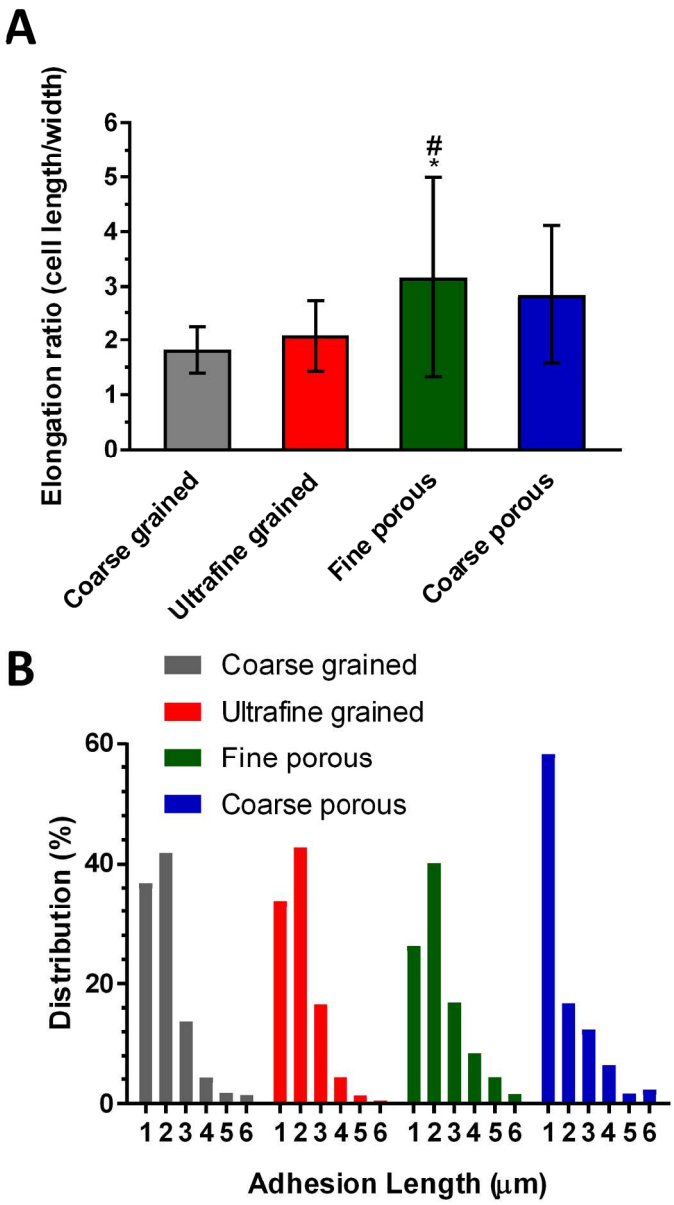

Fig. 10. (A): elongation ratio (cell long axis/short axis) and (B): the length distribution of focal adhesions on various Ti-20Mo substrates after culturing for 8 days (mean ± SD, *: $p < 0.05$ vs. coarse-grained surfaces, #: $p < 0.05$ vs. ultrafine-grained surfaces).

140x250mm (300 x 300 DPI)

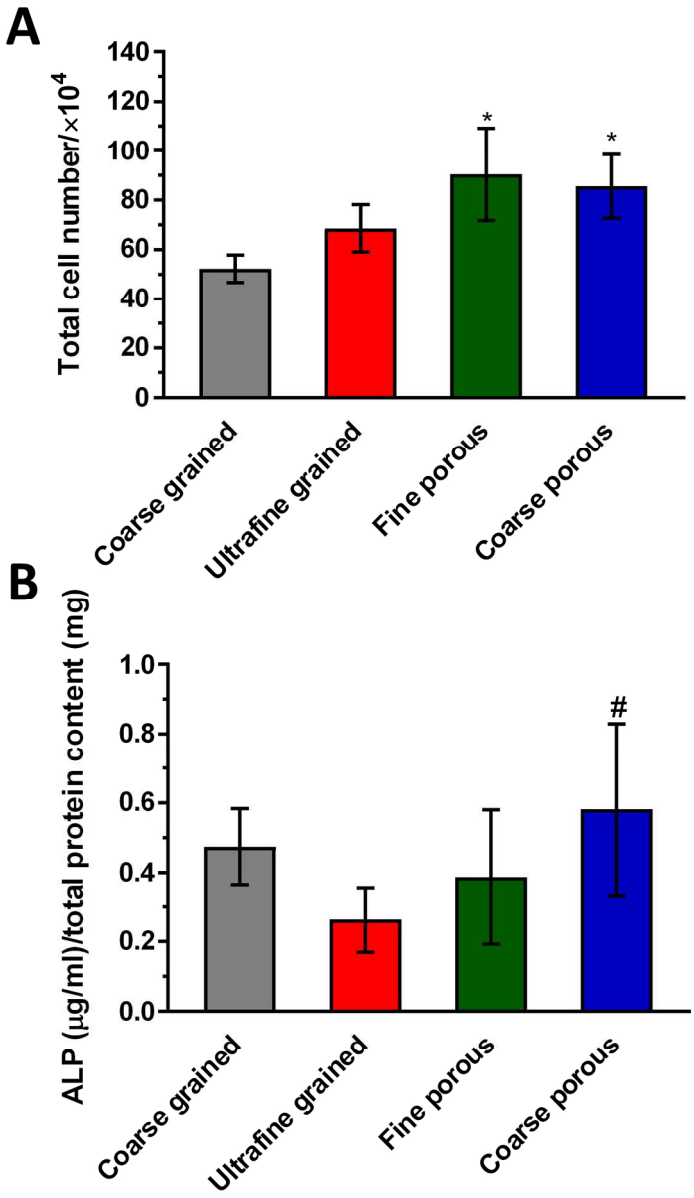

Fig. 11. (A): total cell number and (B): ALP activity normalised to protein content of osteoblasts cultured on different Ti-20Mo surfaces for 8 days. (mean ± SD, * $p < 0.05$ vs. coarse-grained surfaces, #: $p < 0.05$ vs. ultrafine-grained surfaces).

131x227mm (300 x 300 DPI)